# Supplementary Information

## Intrinsic room-temperature ferromagnetism in a two-dimensional semiconducting metal-organic framework

Sihua Feng,[1] Hengli Duan,[1,*] Hao Tan,[1] Fengchun Hu,[1] Chaocheng Liu,[1] Yao Wang,[1] Zhi Li,[1] Liang Cai,[1] Yuyang Cao,[1] Chao Wang,[1,*] Zeming Qi,[1] Li Song,[1] Xuguang Liu,[2] Zhihu Sun[1] and Wensheng Yan[1,*]

[1]*National Synchrotron Radiation Laboratory, University of Science and Technology of China, 230026 Hefei, Anhui, China*
[2]*Hefei National Laboratory for Physical Sciences at the Microscale, University of Science and Technology of China, 230026 Hefei, Anhui, China*

**Corresponding Author**
* Hengli Duan — Email: hlduan@ustc.edu.cn
* Chao Wang — Email: chaowng@ustc.edu.cn
* Wensheng Yan — Email: ywsh2000@ustc.edu.cn

## Supporting Figures

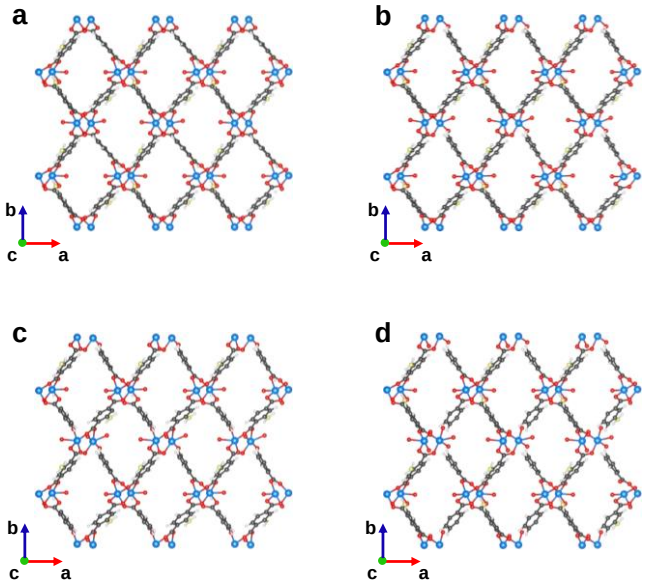


**Supplementary Figure 1. Structure models of Cu-MOFs.** Structure models of the Cu-ABDC (**a**), 1.4%-LS-Cu-ABDC (**b**) and 2.7%-LS-Cu-ABDC at diagonal (**d**) and adjacent (**d**), respectively. Copper, carbon, nitrogen, oxygen and hydrogen atoms are shown in blue, gray, yellow, red and white, respectively, and the axial solvent molecules are omitted for clarity in all structure models.

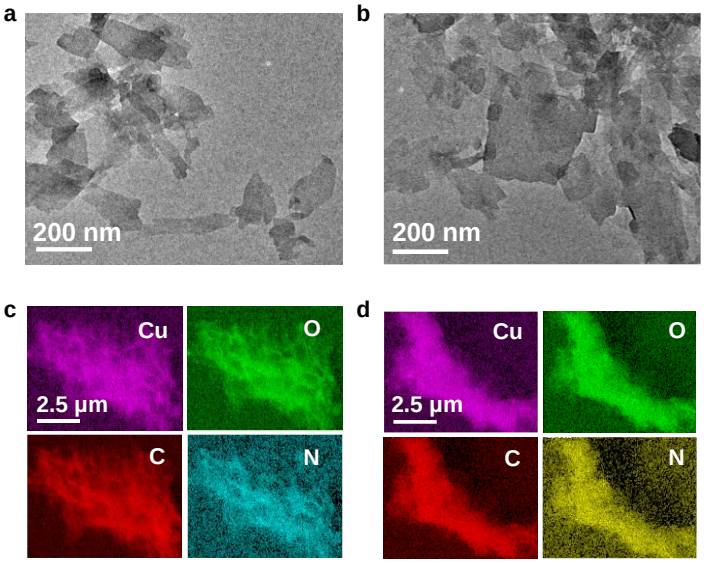


**Supplementary Figure 2. TEM characterizations. a-b**, TEM images of 1.4%-LS-Cu-ABDC and 2.7%-LS-Cu-ABDC nanosheets. **c-d**, Corresponding mapping images of 1.4%-LS-Cu-ABDC and 2.7%-LS-Cu-ABDC.

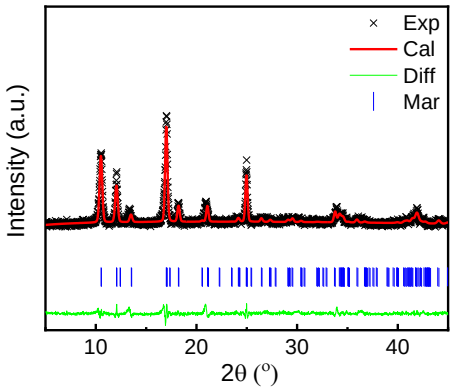


**Supplementary Figure 3. XRD characterizations.** XRD pattern of Cu-ABDC compared to the reference.[1] Considering that the presence of the distinct sequences of functionalities along the MOF backbone will cause an abundant pore environment, and will not change the crystal structure of the MOF.[2, 3] Therefore, we synthesized the Cu-ABDC using 2-amino-1,4-benzenedicarboxyulic acid (ABDC) and $Cu(NO_3)_2 \cdot 3H_2O$, and the crystal structure is exactly consistent with that of well-known Cu(tpa)·DMF.[1] We also have carried out the Rietveld refined XRD pattern of the Cu-ABDC MOF using the software Rietica. As seen from Figure S3, all peaks of the MOF are indexed to the standard structure Cu(tpa)·DMF MOF with space group *C* 2/m (CCDC-687690), which is synthesized using 1,4-benzenedicarboxyulic acid (BDC) and $Cu(NO_3)_2 \cdot 3H_2O$ and has been reported by Carson *et al.*,[1, 2, 3, 4, 5] suggesting the Rietveld refinement of the XRD data reveals an almost single-phase nature of the MOF. The lattice parameters of the MOF obtained from the refinement are $a$ = 11.1345 Å, $b$ = 14.2439 Å and $c$ = 7.8529 Å, which is basically in agreement with the value reported by Carson *et al.*, indicating a reliable quality for our sample.

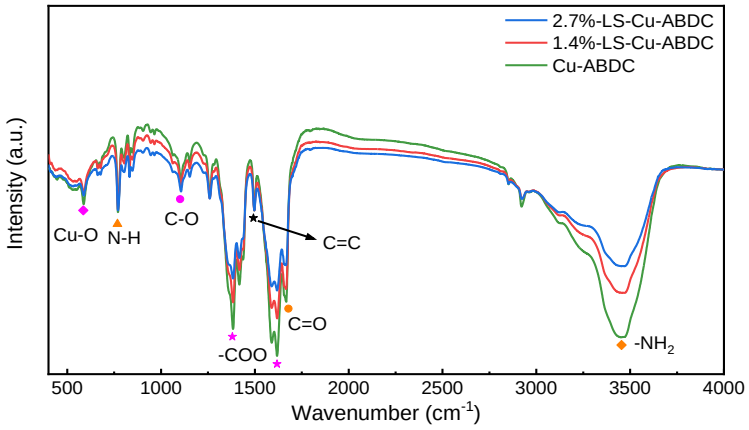


**Supplementary Figure 4. FT-IR analysis.** The curves of all the samples are normalized by the vibration intensity of C=C for the same of the amount of the organic ligand. For all the Cu-MOFs, the peak at about 3482 $cm^{-1}$ is clearly observed which is ascribed to the asymmetrical stretching vibration adsorption of the amine groups. In the lower frequency region, the peaks at about 1590, 1507 and 1259 $cm^{-1}$ correspond to the N-H, C-H and C-N bending vibrations, respectively. The peaks at about 1101, 1500 and 1668 $cm^{-1}$ are ascribed to the vibrations of C-O, C=C stretching of the benzene ring and C=O of solvent molecule.[6] In addition, two peaks at ~1384 and 1619 $cm^{-1}$ are assigned to the symmetric and asymmetric vibrations of the -COO groups, confirming the existence of ligand in Cu-MOFs skeleton.[7, 8] Besides, a characteristic peak at about 580 $cm^{-1}$ can be assigned to Cu-O stretching, suggesting that organic ligands are efficiently coordinated to Cu atoms to form Cu-MOFs. Moreover, the vibration intensities of -COO gradually decrease with the increase of ligand cleavages after the normalization with the signals of C=C, suggesting the missing of organic linkers.

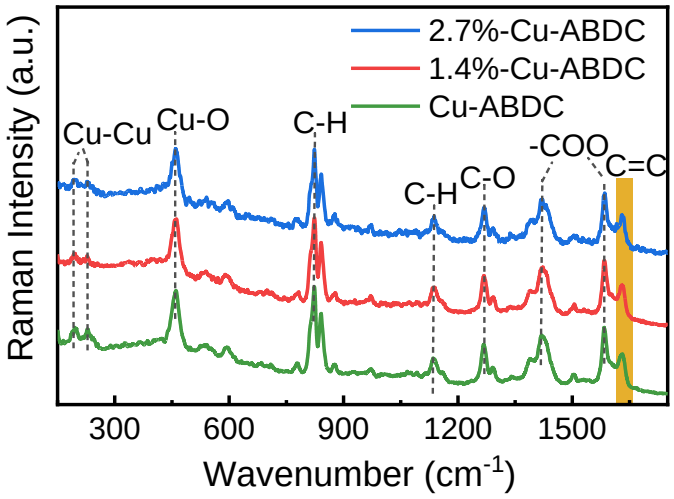


**Supplementary Figure 5. Raman spectroscopy analysis.** The vibration intensity of all the peaks are normalized by the vibration intensity of C=C at about 1633 $cm^{-1}$ for the same of the amount of the organic ligand. In the low-frequency region, a doublet at about 194 and 229 $cm^{-1}$ are assigned to Cu-Cu stretching modes. At about 460 $cm^{-1}$, Cu-O stretching mode is detected, which indicates that Cu ions coordinate with ligands and the successfully synthesis of the Cu-MOFs.[9] The peaks at ~ 820 and 1130 $cm^{-1}$ represent the vibrations of C-H in Cu-MOFs. In addition, a peak at about 1267 $cm^{-1}$ is attributed to C-O bond. Two peaks at about 1420 and 1584 $cm^{-1}$ are dominated by the vibrations of -COO groups, and the band at about 1633 $cm^{-1}$ is assigned to C=C stretching mode.[10, 11] Meanwhile, a new band can be discovered at about 1137 $cm^{-1}$, likely owing to a deformation mode involving the carboxylate group coupled with a C-C stretching mode.[12] It is worth noting that the vibration intensities of -COO gradually decrease with the ligand cleavages, which further confirms the missing organic linkers.

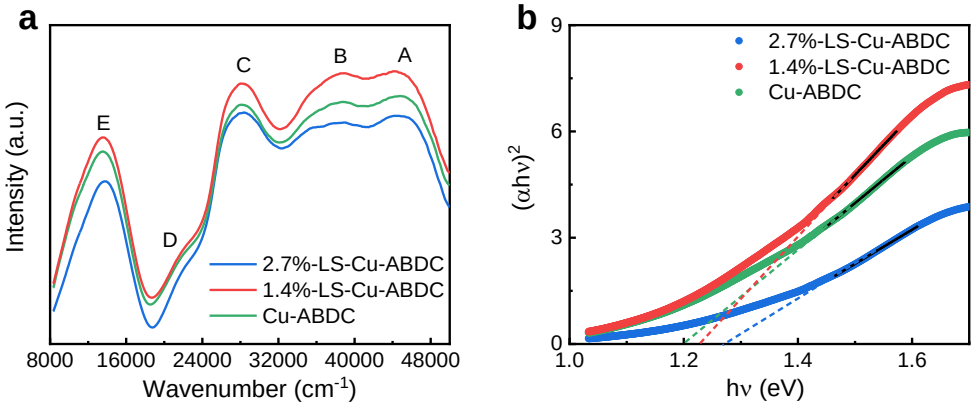


**Supplementary Figure 6. UV/Vis spectra of Cu-MOFs.** Two absorption peaks D (21453 $cm^{-1}$) and E (13609 $cm^{-1}$) can be detected, which are attributed to charge transfer between ligand and metal and metal-radical spin-exchange originated from *d-d* transition.[13] There also present three peaks A (45610 $cm^{-1}$), B (38021 $cm^{-1}$) and C (27934 $cm^{-1}$), which may be ascribed to the transition of the $\pi \rightarrow \pi^*$ of the organic functional groups, the transition of the $\pi \rightarrow \pi^*$ of the aromatic rings and the electron transfer transition from ligand to metal.[12, 14, 15] Moreover, bandgaps are fitted as 1.20, 1.22 and 1.27 eV for Cu-ABDC, 1.4%-LS-Cu-ABDC and 2.7%-LS-Cu-ABDC, respectively, suggesting its semiconductor behaviors and the bandgaps gradually increase with the ligand cleavages, in agreement with theoretical calculation results below.

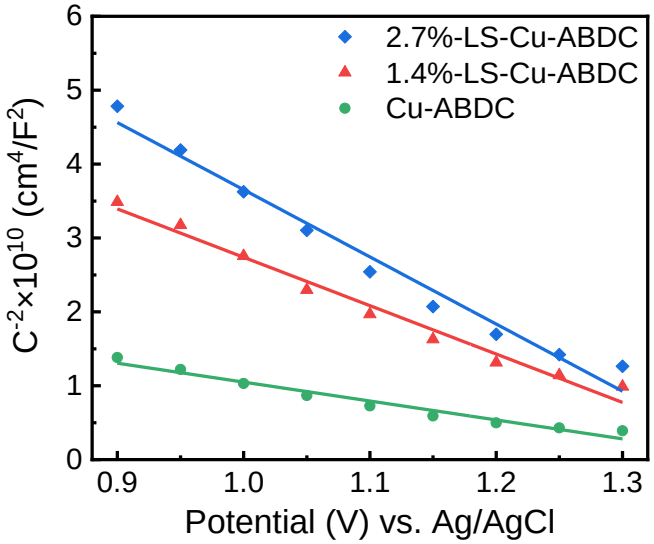


**Supplementary Figure 7. Mott-Schottky plots of Cu-MOFs.** Mott-Schottky analysis was carried out in the linear region of the $C^{-2}$ curve from 0.9 to 1.3 V vs Ag/AgCl with frequency of 2 kHz in 1 M KOH.[16, 17] All the Cu-MOFs exhibit *p*-type semiconductor character, in agreement with theoretical calculation results, and the hole carrier density of Cu-ABDC is about 2.5 and 3.5 time larger than that of the 1.4%-LS-Cu-ABDC and 2.7%-LS-Cu-ABDC, respectively.

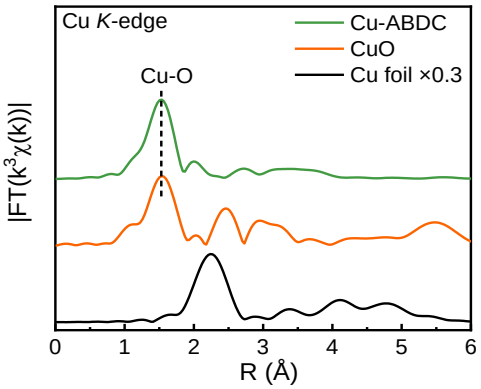


**Supplementary Figure 8. Cu *K*-edge EXAFS**. Cu *K*-edge EXAFS curves including Cu foil and CuO as reference samples indicate the Cu-O coordination in Cu-ABDC.

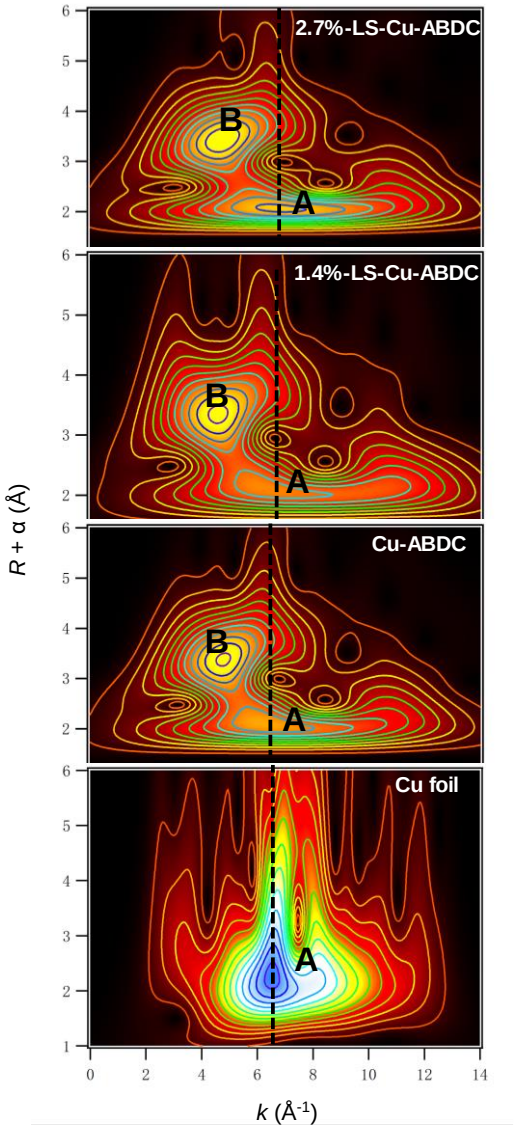


**Supplementary Figure 9. Wavelet transform (WT) analysis of Cu-MOFs.** After filtering out the coordination of Cu-O in the first shell, the WT of Cu K-edge EXAFS data of Cu-MOFs show a maximum A at the cross-point of about $R_A$ = 2.1 Å/$k_A$ = 6.3 $Å^{-1}$, which is close to that of Cu foil, confirming that the second shell arises from the coordination of Cu-Cu, in agreement with the EXAFS fitting results. Furthermore, the maximum B at about $R_A$ = 3.4 Å/$k_A$ = 4.3 $Å^{-1}$ may be from the multiple shell scattering or higher shell contribution of Cu-C coordination.

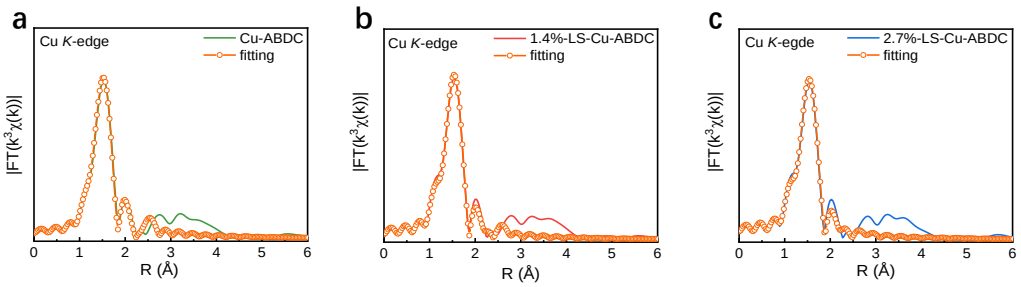


**Supplementary Figure 10. Cu *K*-edge EXAFS fitting curves in *R*-space.** Cu *K*-edge EXAFS fitting curves in *R*-space of Cu-ABDC (**a**), 1.4%-LS-Cu-ABDC (**b**), 2.7%-LS-Cu-ABDC (**c**), respectively. The fitted *R* range here is from 1.1 to 2.4 Angstroms.

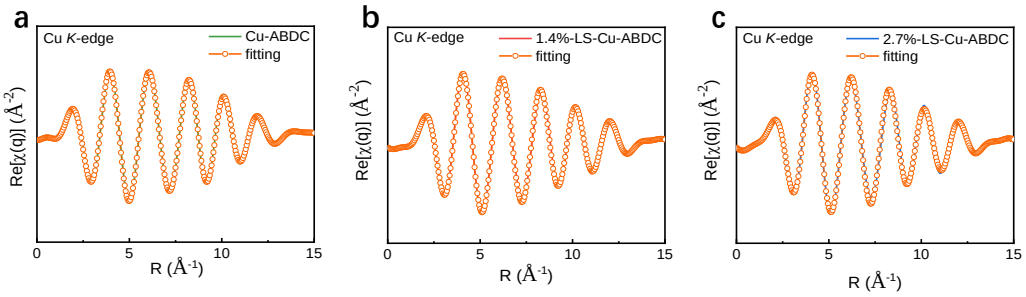


**Supplementary Figure 11. Cu *K*-edge EXAFS fitting curves in *q*-space.** Cu *K*-edge EXAFS fitting curves in *q*-space of Cu-ABDC (**a**), 1.4%-LS-Cu-ABDC (**b**) and 2.7%-LS-Cu-ABDC (**c**), respectively.

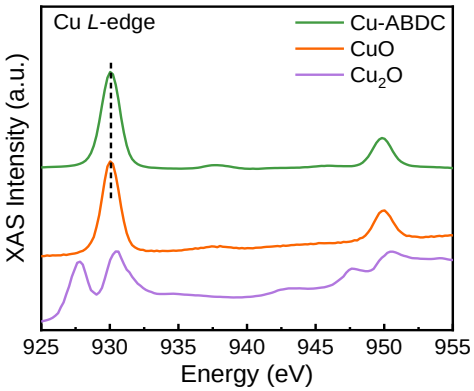


**Supplementary Figure 12. Cu *L*-edge XAS.** Cu *L*-edge XAS for Cu-ABDC including $Cu_2O$ and CuO as reference samples suggests +2 valence state of Cu ions in Cu-ABDC.

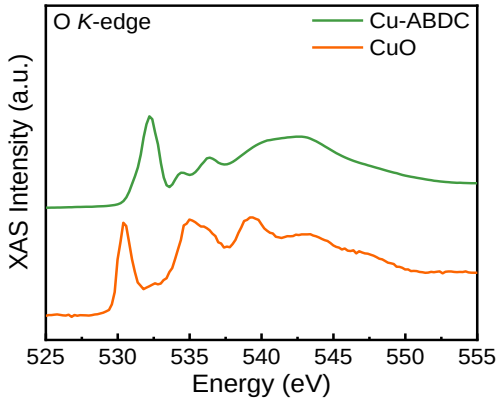


**Supplementary Figure 13. O *K*-edge XAS.** O *K*-edge XAS of Cu-ABDC and the reference sample CuO. Two regions can be directly detected from O *K*-edge, a sharp π* region around 530 eV origins from the electrons excited into O 2*p* orbitals hybridized with Cu 3*d*, and the σ* region at about 540 eV is mainly from the electrons excited into O 2*p* orbitals that are hybridized with Cu 4sp and C 2*sp*.[18, 19, 20] O *K*-edge of Cu-ABDC is different from that of CuO because oxygen atoms connect not only with Cu ions but also with benzene ring, which further confirms the synthesis of Cu-ABDC and the absence of CuO.

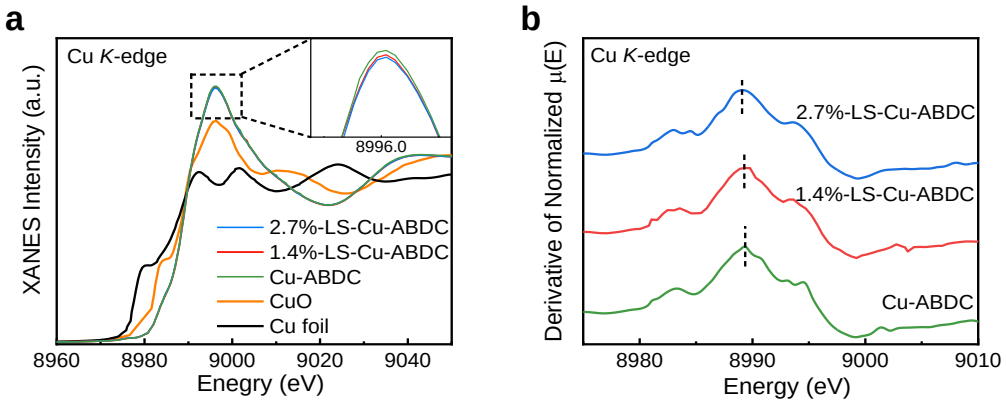


**Supplementary Figure 14. Cu *K*-edge XANES curves. a**, Cu *K*-edge XANES curves of Cu-MOFs and the reference samples. **b**, Cu *K*-edge first-derivative XANES curves of Cu-MOFs. The absorption edge positions of Cu-MOFs are close to that of CuO, indicating +2 valence state of Cu ions in Cu-MOFs. The decreased absorption intensities of white-line peaks at about 8996 eV and the lower-energy shifts of Cu *K*-edge first-derivative XANES further confirm that the electron occupation of Cu 3*d* states gradually increase with the increase of ligand cleavage.

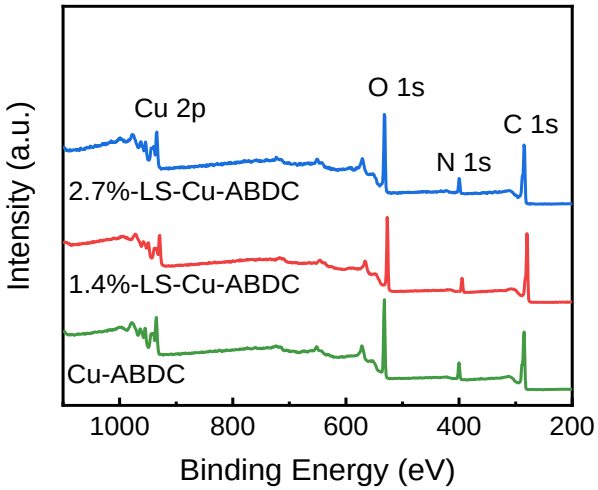


**Supplementary Figure 15**. **XPS survey analysis**. XPS survey analysis reveals that there are only Cu, N, O, C elements in Cu-MOFs without other magnetic impurities.

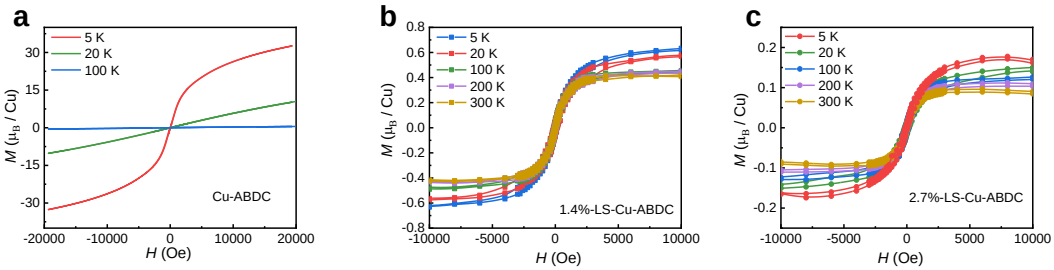


**Supplementary Figure 16. The *M-H* curves at different temperatures for Cu-MOFs.** *M-H* curves of 1.4%-LS-Cu-ABDC (**a**) and 2.7%-LS-Cu-ABDC (**b**), respective. According to our synthesized method, the substitution of ligands is hard to precisely control and hence not uniform during sample preparation. It is possible that antiferromagnetic coupling remains in some Cu dimers whose ligands are not replaced, so the magnetic moment is smaller than 1$\mu_B$/Cu atom.

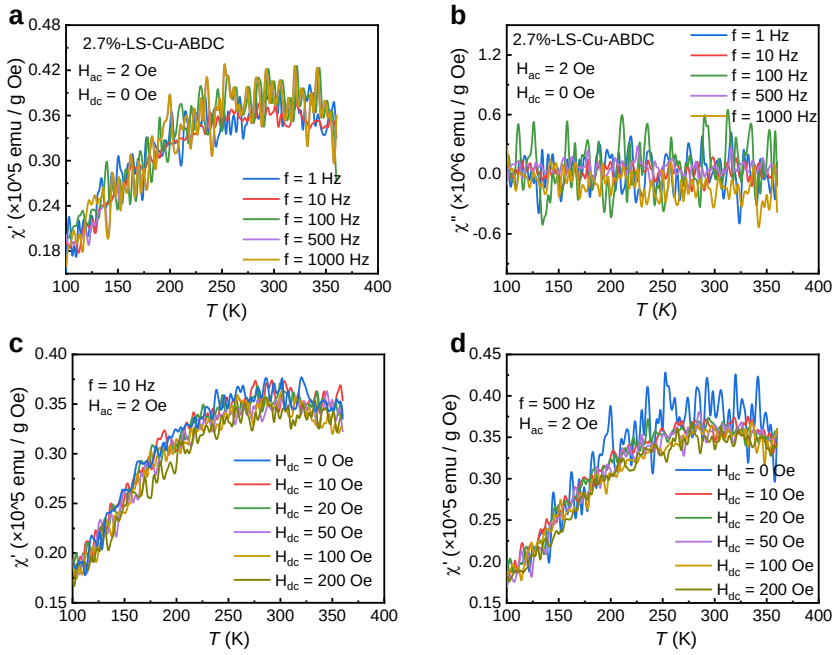


**Supplementary Figure 17. AC magnetic susceptibility measurement of 2.7%-LS-Cu-ABDC MOF.** (**a-b**) Temperature variation of the real part of the ac susceptibility measurement (**a**) and imaginary part (**b**) at various frequencies from 1 Hz to 1000 Hz with $H_{ac}$ = 2 Oe and $H_{dc}$ = 0 Oe from 100 to 360 K. (**c-d**) Temperature variation of the real part of the ac susceptibility measurement at various $H_{dc}$ from 0 Oe to 200 Oe with $H_{ac}$ = 2 Oe and $f$ = 10 Hz (**c**) and 500 Hz (**d**) from 100 to 360 K.

In order to further investigate the possibility of a glassy state, we preformed the real part of AC magnetic susceptibility $\chi'(T)$ (dispersion) for 2.7%-LS-Cu-ABDC MOF as a function of temperature at an AC field of $H_{ac}$ = 2 Oe and $H_{dc}$ = 0 Oe with several frequencies ($f$ = 1, 10, 100, 500, and 1000 Hz) at the temperature range of 100-360 K. However, the peak positions at about 275 K have no obvious changes with the frequency. Moreover, the imaginary part $\chi''$ (absorption) remains practically zero. On the other hand, we also measured the real part of AC magnetic susceptibility $\chi'(T)$ for 2.7%-LS-Cu-ABDC MOF as a function of temperature at an AC field of $H_{ac}$ = 2 Oe with several DC field ($H_{dc}$ = 0, 10, 20, 50, 100 and 200 Oe) at temperature range 100-360 K under $f$ = 10 and 500 Hz, respectively. The peak positions also remain unchanged at different DC fields. These results indicate no obvious spin glass signal in our samples. The above results lead to the conclusion of complete absence of spin glass state.[21, 22, 23]

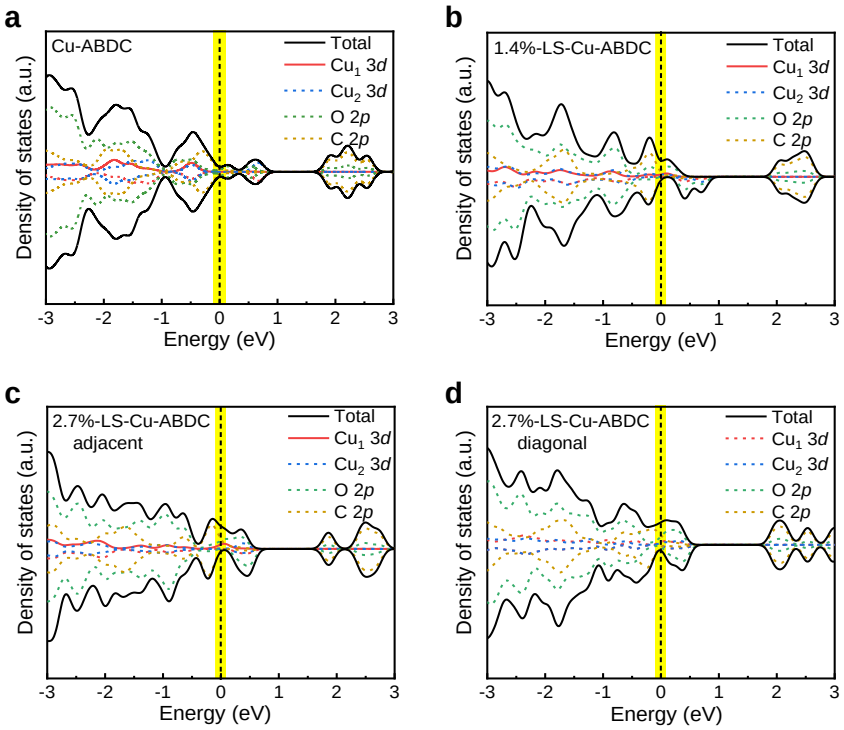


**Supplementary Figure 18. Theoretical calculation**. The calculated densities of states (DOS) for Cu-ABDC (**a**), 1.4%-LS-Cu-ABDC (**b**) and 2.7%-LS-Cu-ABDC (**c-d**), respectively. DFT calculations reveal that the long-range ferromagnetic interaction between adjacent dimers mainly arises from the hybridization between Cu 3*d*, O 2*p* and C 2*p* orbitals.

## Supplementary Tables

**Supplementary Table 1. Inductively coupled plasma atomic emission spectroscopy (ICP-AES) results.** There are no other magnetic impurities in our samples, excepting $Cu^{2+}$ ions, and the concentration of the Cu ions remain nearly unchanged in our MOF. The initial sample concentration was 10 mg / L. Based on the chemical formal $Cu_2$(ABDC)·2DMF, the theoretical mass ratio of Cu ions is 28%, which is closed to our experiment results.

| Sample | Cu-ABDC | 1.4%-LS-Cu-ABDC | 2.7%-LS-Cu-ABDC |
|---|---|---|---|
| Element | Cu | Cu | Cu |
| Concentration. mg/L | 3.06 | 2.93 | 2.89 |

**Supplementary Table 2. Cu *K*-edge EXAFS fitting results for Cu-MOFs.**

| Sample | Path | *N* | *R* (Å) | $\sigma^2$ (Å$^2$) | $\Delta E_0$ | *R* |
|---|---|---|---|---|---|---|
| Cu-ABDC | Cu-$O_1$ | 4±0.4 | 1.95±0.01 | 0.0057±0.001 | -7.1±0.8 | 0.000058 |
| | Cu-$O_2$ | 1.2±0.1 | 1.98±0.01 | 0.003±0.001 | | |
| | Cu-Cu | 1±0.1 | 2.67±0.02 | 0.012±0.003 | | |
| 1.4%-LS-Cu-ABDC | Cu-$O_1$ | 3.7±0.3 | 1.95±0.01 | 0.005±0.001 | -2.0±1.6 | 0.00015 |
| | Cu-$O_2$ | 1.3±0.1 | 1.98±0.01 | 0.004±0.001 | | |
| | Cu-Cu | 1±0.1 | 2.72±0.01 | 0.015±0.007 | | |
| 2.7%-LS-Cu-ABDC | Cu-$O_1$ | 3.4±0.3 | 1.96±0.01 | 0.0047±0.001 | -3.2±10.6 | 0.00074 |
| | Cu-$O_2$ | 1.7±0.2 | 1.98±0.01 | 0.004±0.001 | | |
| | Cu-Cu | 1±0.1 | 2.75±0.01 | 0.018±0.003 | | |

*N*, coordination number; *R*, bonding distance; $\sigma^2$, Debye-Waller factor; $\Delta E_0$, inner potential shift; *R* factor reveals the goodness of the fit. The fitted *R* range here is from 1.1 to 2.4 Angstroms.

**Supplementary Table 3. DFT calculation results of Cu-ABDC and LS-Cu-ABDC with solvent molecules.**

| Sample | Structure | $E_{FM}$ (eV) | $E_{AFM}$ (eV) | $\Delta E_{FM\text{-}AFM}$ (eV) | Magetic momet ($\mu_B$) | $d_{Cu\text{-}Cu}$ (Å) |
|---|---|---|---|---|---|---|
| Cu-ABDC | 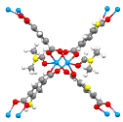 | -52720.775 | -52720.893 | 0.118 | 0.57 | 2.588 |
| 1.4%-LS-Cu-ABDC | 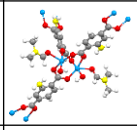 | -52516.939 | -52516.912 | -0.027 | 0.32 | 2.693 |
| 2.7%-LS-Cu-ABDC (adjacent) | 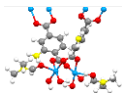 | -52312.844 | --- | --- | 0.1 | 2.731 |
| 2.7%-LS-Cu-ABDC (diagonal) | 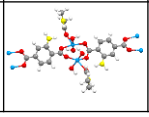 | -52312.569 | --- | --- | 0.04 | 2.910 |

$\Delta E$ defined as the difference in energy between the FM and AFM spin configurations: $\Delta E = E_{FM} - E_{AFM}$. The signal "---" represents the absence of antiferromagnetic state. Copper, carbon, nitrogen, oxygen and hydrogen atoms are shown in blue, gray, yellow, red and white, respectively.

## References


1. Carson CG*, et al.* Synthesis and Structure Characterization of Copper Terephthalate Metal-Organic Frameworks. *Eur. J. Inorg. Chem.* **16**, 2338-2343 (2009).
2. Hexiang Deng CJD, Hiroyasu Furukawa, Ricardo B. Ferreira, John Towne, Carolyn B. Knobler, Bo Wang, Omar M. Yaghi. Multiple Functional Groups of Varying Ratios in Metal-Organic Frameworks. *Science* **327**, 846-850 (2010).
3. Braun ME, Steffek CD, Kim J, Rasmussen PG, Yaghi OM. 1,4-Benzenedicarboxylate derivatives as links in the design of paddle-wheel units and metal-organic frameworks. *Chem. Commun.*, 2532-2533 (2001).
4. Rodenas T*, et al.* Metal-organic framework nanosheets in polymer composite materials for gas separation. *Nat. Mater.* **14**, 48-55 (2015).
5. Zhan G*, et al.* Fabrication of Ultrathin 2D Cu-BDC Nanosheets and the Derived Integrated MOF Nanocomposites. *Adv. Funct. Mater.* **29**, (2019).
6. Zhang W*, et al.* Dynamic Restructuring of Coordinatively Unsaturated Copper Paddle Wheel Clusters to Boost Electrochemical $CO_2$ Reduction to Hydrocarbons. *Angew. Chem. In.t Ed. Engl* **61**, e202112116 (2022).
7. Zhao M*, et al.* Core-shell palladium nanoparticle@metal-organic frameworks as multifunctional catalysts for cascade reactions. *J. Am. Chem. Soc.* **136**, 1738-1741 (2014).
8. Zhang YW, Li Z, Zhao Q, Zhou YL, Liu HW, Zhang XX. A facilely synthesized amino-functionalized metal-organic framework for highly specific and efficient enrichment of glycopeptides. *Chem. Commun.* **50**, 11504-11506 (2014).
9. Dhumal NR, Singh MP, Anderson JA, Kiefer J, Kim HJ. Molecular Interactions of a Cu-Based Metal-Organic Framework with a Confined Imidazolium-Based Ionic Liquid: A Combined Density Functional Theory and Experimental Vibrational Spectroscopy Study. *J. Phys. Chem. C* **120**, 3295-3304 (2016).
10. Deng X*, et al.* Metal-Organic Framework Coating Enhances the Performance of Cu2O in Photoelectrochemical $CO_2$ Reduction. *J. Am. Chem. Soc.* **141**, 10924-10929 (2019).
11. C. Prestipino LR, J. G. Vitillo, F. Bonino A. Damin, C. Lamberti A. Zecchina, P. L. Solari, K. O. Kongshaug, and S. Bordiga. Local Structure of Framework Cu(II) in HKUST-1 Metallorganic Framework: Spectroscopic Characterization upon Activation and Interaction with Adsorbates. *Chem. Mater.* **18**, 1337-1346 (2006).
12. Bordiga S*, et al.* Electronic and vibrational properties of a MOF-5 metal-organic framework: ZnO quantum dot behavior. *Chem. Commun.*, 2300-2301 (2004).
13. Ziebel ME, Darago LE, Long JR. Control of Electronic Structure and Conductivity in Two-Dimensional Metal-Semiquinoid Frameworks of Titanium, Vanadium, and Chromium. *J. Am. Chem. Soc.* **140**, 3040-3051 (2018).
14. Xiao JD, Han L, Luo J, Yu SH, Jiang HL. Integration of Plasmonic Effects and Schottky Junctions into Metal-Organic Framework Composites: Steering Charge Flow for Enhanced Visible-Light Photocatalysis. *Angew. Chem. Int. Ed.*

*Engl* **57**, 1103-1107 (2018).
15. Darago LE, Aubrey ML, Yu CJ, Gonzalez MI, Long JR. Electronic Conductivity, Ferrimagnetic Ordering, and Reductive Insertion Mediated by Organic Mixed-Valence in a Ferric Semiquinoid Metal-Organic Framework. *J. Am. Chem. Soc.* **137**, 15703-15711 (2015).
16. Goncalves RH, Lima BH, Leite ER. Magnetite colloidal nanocrystals: a facile pathway to prepare mesoporous hematite thin films for photoelectrochemical water splitting. *J. Am. Chem. Soc.* **133**, 6012-6019 (2011).
17. Luo W, Wang J, Zhao X, Zhao Z, Li Z, Zou Z. Formation energy and photoelectrochemical properties of $BiVO_4$ after doping at $Bi^{3+}$ or $V^{5+}$ sites with higher valence metal ions. *Phys. Chem. Chem. Phy.s* **15**, 1006-1013 (2013).
18. Suntivich J*, et al.* Estimating Hybridization of Transition Metal and Oxygen States in Perovskites from O K-edge X-ray Absorption Spectroscopy. *J. Phys. Chem. C* **118**, 1856-1863 (2014).
19. F. M. de Groot *et al.*, Oxygen 1s x-ray-absorption edges of transition-metal oxides. *Phys. Rev. B* **40**, 5715-5723 (1989).
20. Chen Y*, et al.* Electronic origin of hydrogen storage in MOF-covered palladium nanocubes investigated by synchrotron X-rays. *Commun. Chem.* **1**, (2018).
21. Singh MK, Prellier W, Singh MP, Katiyar RS, Scott JF. Spin-glass transition in single-crystalBiFeO3. *Phys. Rev. B* **77**, (2008).
22. Goremychkin EA, Osborn R, Rainford BD, Macaluso RT, Adroja DT, Koza M. Spin-glass order induced by dynamic frustration. *Nat. Phys.* **4**, 766-770 (2008).
23. Mustonen O, *et al.* Spin-liquid-like state in a spin-1/2 square-lattice antiferromagnet perovskite induced by $d^{10}$-$d^0$ cation mixing. *Nat. Commun.* **9**, 1085 (2018).